ARCHIVES
of
FOUNDRY ENGINEERING

ISSN (2299-2944)
Volume 2026
Issue 1/2026

84 – 92

9/1

10.24425/afe.2026.157972

Published quarterly as the organ of the Foundry Commission of the Polish Academy of Sciences

Research on Stirring Characteristics of Molten Bath with Swirl-Type Oxygen Lance for Large Scale Converter

Qiang Fu [a], Xi Wang [b,*], Guang qiang Liu [b], Kun Liu [c]
[a] Beiying Steelmaking Plant, Benxi Steel Group, China
[b] College of Civil Engineering, University of Science and Technology Liaoning, China
[c] School of Materials and Metallurgy, University of Science and Technology Liaoning, China
* Corresponding author: e-mail: wangx5033@sina.com

Received 12.09.25; accepted in revised form 05.12.25; available online 30.03.2026

Abstract

In the modern steelmaking, the impact behaviour of supersonic oxygen jet on the molten bath is vital importance for the refining process. The impact characteristics and flow field distribution of molten bath for swirl-type oxygen lance in 260 Mg converter were analyzed by physical experiments and numerical simulations, and industrial test research was conducted. These results demonstrate that compared to the traditional oxygen lance, the cavity depth, cavity width and mixing time of swirl-type oxygen lance decrease, increase and decrease, respectively. The mixing efficiency of molten bath for swirl-type oxygen lance is improved by 5.5% to 16.8%. The optimal operation parameters of swirl-type oxygen lance for 260 Mg converter are H=40d_e and Q=80 Nm^3·h^{-1}. When the swirl angle is 10 °, the molten bath obtains the maximum volume-average velocity, the minimum dead zone volume and the shortest mixing time. Industrial test shown that compared with traditional oxygen lance, the swirl-type oxygen lance increased the dephosphorization rate by 2.3%, decreased the final carbon content by 0.005%, and decreased the iron content of final slag by 0.11%. The findings of this work can provide a basic reference for the industrial application of swirl-type oxygen lance in large-scale converter.

Keywords: Swirl-type oxygen lance, Mixing time, Volume of dead zone, Industrial test

1. Introduction

Converter steelmaking is a core process in modern steelmaking. The improvement of converter production efficiency and technology is of great significance to the development of steel enterprises. As a key equipment for converter steelmaking, the oxygen lance is used to transfer oxygen in the form of a supersonic jet into the molten bath, and provide good dynamic conditions for slagging, decarbonization, and dephosphorization [1-3]. Therefore, the performance of the oxygen lance is crucial for converter steelmaking [4-6]. In recent years, domestic and foreign researchers have conducted extensive research on the influence of traditional oxygen lance jet on the stirring effect of the molten bath.

Lv et al. [7] studied the influences of oxygen flow rate, lance height, and slag thickness on the flow of molten steel based on a three-dimensional mathematical model of a 100 Mg converter. Li et al. [8] investigated the impact behaviour of multiple jets on the molten bath based on the gas-slag-metal VOF (Volume of Fluid) model, and found that the cavity depth increased with the increase of operating pressure, but the cavity width was almost unaffected by the operating pressure. Ek et al. [9] conducted cold model experiments using liquid alloy Ga-In-Sn and found that the velocity of the droplet was found to be at a level only about 1% of the

terminal velocity. Based on cold model experiments, Sabah et al. [10] estimated the energy consumption of different parts of the steelmaking gas injection process and found that dissipation and splashing are the dominant processes where most of the power of the jet is used, whereas cavity formation consumes the least amount. Li et al. [11] conducted numerical research on the dynamic characteristics of supersonic jets in a swirl-type oxygen lance and found that increasing the swirl angle resulted in weaker jet coalescence, thereby improving the heat transfer efficiency between the jet and the surrounding environment. Maia et al. [12] compared the effects of twisted nozzle, flow and lance height in the jet penetration through experiments, and found that high flow, reduction in bath lance distance and lower nozzle angle promoted a higher penetration. Yin et al. [13] studied the emulsification and stirring effects of gas-slag-metal for the swirl-type oxygen lance blowing process. The results showed that an appropriate swirling angle can improve the stirring efficiency and accelerate the slagging reaction. Lv et al. [14] established a three-dimensional gas-slag-metal model of a 120 Mg converter and studied the changes in jet characteristics during the swirl-type oxygen lance blowing process. It was found that as the swirl angle increased, the length of the high-velocity zone, maximum velocity, and dynamic pressure of the jet decreased. Based on physical experiment, Li et al. [15] found swirl-type oxygen lance with a swirl angle of 20 ° performs the best in splashing and stirring ability of molten bath. However, the size of converter is medium in above studies, and fewer studies have been carried out on the application of swirl-type oxygen lance in large-scale converter.

In the study, the impact behavior and flow field distribution of molten bath for swirl-type oxygen lance with various swirl angles in 260 Mg converter were studied. The cavity depth, cavity width and mixing time were measured by physical experiment. The velocity distribution and dead zone of molten bath were analyzed by numerical simulation. Industrial experimental research was conducted in a 260 Mg converter. The findings of this work can provide a basic reference for the industrial application of swirl-type oxygen lance in large-scale converter.

2. Numerical modelling

2.1. Assumptions

1) Gas phase was considered a compressible ideal gas and liquid phase was regarded as an incompressible Newtonian fluid.
2) Viscosity and surface tension of each phase were regarded as constant.
3) A no-slip condition was applied to the wall, and the heat transfer process did not occur.
4) All chemical reactions of molten bath during the steelmaking process are not considered.

2.2. VOF modelling

To describe the interaction between gas-liquid multiphase flow interfaces in the converter, the VOF model was adopted in the study [16]. In the VOF mode, all variables are calculated based on the Reynolds averaged Navier Stokes (RANS) equation. The continuity equation and momentum equation are as follows:

$$\frac{\partial \alpha_q \rho_q}{\partial t} + \nabla\left(\alpha_q \rho_q \vec{v}\right) = 0 \tag{1}$$

where α_q is the volume fraction of phase q, ρ_q is the density of phase q (kg/m^3); $\vec{v}$ is the velocity (m/s); and t is time (s).

$$\frac{\partial}{\partial t}\left(\rho\vec{v}\right) + \nabla\cdot\left(\rho\vec{v}\vec{v}\right) = \nabla p + \nabla\cdot\left[\mu\left(\nabla\vec{v} + \nabla\vec{v}^T\right)\right] + \rho\vec{g} + \vec{F} \tag{2}$$

where p is the static pressure (Pa); g is the gravitational acceleration (m/s^2); and $\vec{F}$ is the volume force (N). In the model, the surface tension effect is considered as body forces:

$$\vec{F} = \int_V \sigma K \nabla\alpha dV = \sigma K_f\left(\nabla\alpha_f\right)V_f \tag{3}$$

where V_f is the volume of grid f (m^3), σ is the surface tension coefficient, and K is the curvature (1/m). The curvature is expressed as follows:

$$K_f = -\left(\nabla\cdot\hat{n}\right) = -\left[\nabla\cdot\left(\frac{\nabla\alpha}{|\nabla\alpha|}\right)\right]_f \tag{4}$$

where $\hat{n}$ is the unit vector normal to the surface.

The physical properties of fluid are calculated based on the average volume of the phases. For instance, the density and viscosity of the fluid in each grid are derived by the equations:

$$\rho = \sum_{q=1}^{n} \rho_q \alpha_q \tag{5}$$

$$\mu = \sum_{q=1}^{n} \mu_q \alpha_q \tag{6}$$

where the μ_q is the viscosity of phase q (kg/m^3).

2.3. Turbulence modelling

Compared to the standard k-ε model, the improved realizable k-ε model includes a new formulation for turbulent viscosity and a new transport equation for the dissipation rate ε, which predicts the dissipation rate of jet more accurately. Therefore, the realizable k-ε model was adopted for turbulence calculation [17]. The governing equations for k and ε are as follows:

$$\frac{\partial\left(\rho k\right)}{\partial t} + \frac{\partial\left(\rho k u_j\right)}{\partial x_j} = \frac{\partial}{\partial x_j}\left[\left(\mu + \frac{\mu_t}{\sigma_k}\right)\frac{\partial k}{\partial x_j}\right] + G_k + G_b - \rho\varepsilon - Y_M + S_k \tag{7}$$

$$\frac{\partial\left(\rho\varepsilon\right)}{\partial t} + \frac{\partial\left(\rho\varepsilon u_j\right)}{\partial x_j} = \frac{\partial}{\partial x_j}\left[\left(\mu + \frac{\mu_t}{\sigma_\varepsilon}\right)\frac{\partial\varepsilon}{\partial x_j}\right] + \rho C_1 S\varepsilon - \rho C_2 \frac{\varepsilon^2}{k + \sqrt{\nu\varepsilon}} + C_{1\varepsilon}\frac{\varepsilon}{k}C_{3\varepsilon}G_b + \tag{8}$$

where the parameters G_k and G_b are the generation of turbulent kinetic energy due to mean velocity gradients and buoyancy, respectively; Y_M represents the contribution of fluctuating dilatation in compressible turbulence to the overall dissipation rate; $C_{1\varepsilon}$ and C_2 are constants whose values are 1.44 and 1.92, respectively. When the main flow direction within the buoyant shear layer is along or perpendicular to the gravity direction, the $C_{3\varepsilon}$ is 1 or 0, respectively. σ_k and σ_ε represent the turbulent Prandtl numbers of k and ε with values of 1.0 and 1.2, respectively [18]. μ_t is the turbulent viscosity (Pa·s). v is the kinematic viscosity (m^2/s). S_k and S_ε are the source terms.

2.4. Calculation model and solution process

The process of supersonic oxygen jet impacting the molten bath in a 260 Mg converter was numerically studied. Figure 1a shows the geometric structures of traditional oxygen lance and swirl-type oxygen lance, with their parameters as shown in Table 1. Figure 1b shows that Model A and Model B were established to calculate the flow of single phase and multiphase, respectively [19-21]. Constant state calculation for top-blown free jet was calculated in Model A, and the data such as velocity, static pressure, turbulent kinetic energy, and turbulent dissipation rate from the cross-section of Model A was extracted to import into Model B for transient calculations.

Considering the computational cost, one-fifth of the computational domain was established due to the rotational symmetry of the converter. In the process of grid division, the computational domain is processed using a hexahedral structure, and the local grid optimization is performed at the gas-liquid interface of Model B. The physical parameters of material used are shown in Table 2. The pressure–velocity decoupling was achieved by the press implicit with splitting of operators (PISO) scheme. The interpolation of the pressure values was achieved with the pressure staggering option (PRESTO) algorithm. The compressive interface capturing scheme for arbitrary meshes (CICSAM) was adopted to track the free interface. The transport equations were discretized using a second-order upwind scheme. The initial time step size for Model B was 10^{-5} s. Afterwards, time step size was automatically adjusted based on a global Courant number of 1. The calculation process was considered to be convergent when the residuals of energy equation was less than 1×10^{-6}, and the residuals of other variables were less than 1×10^{-3}.

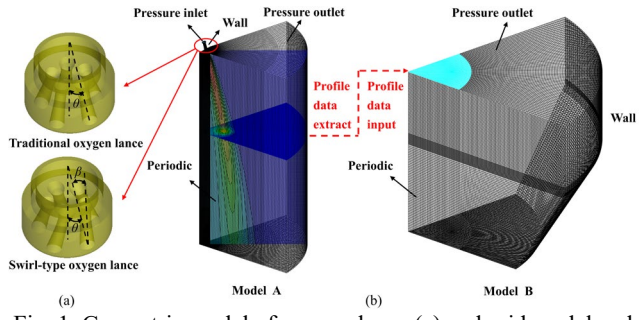

Fig. 1. Geometric model of oxygen lance (a) and grid model and boundary conditions (b)

Table 1.
The parameters of numerical simulation and physical experiment

Parameters	Prototype	Model
Throat diameter, d_t (mm)	45.7	6.53
Outlet diameter, d_e (mm)	61.1	8.73
Inclination angle, α (°)	15	15
Swirl angle, β (°)	0, 5, 8, 10, 12, 15	0, 5, 8, 10, 12, 15
Mach number, Ma (-)	2.07	2.07
Molten bath diameter, D (mm)	6120	875
Molten bath depth, h (mm)	1833	262
Inlet pressure, P_0 (MPa)	0.9	0.9
Back pressure, P_b (MPa)	0.101	0.101
Lance height, H (mm)	1833-3055	261.8-436.4
Top blowing rate, Q (Nm^3/h)	45000-57000	70-90
Bottom blowing rate, Q_b (Nm^3/h)	480	1.6

Table 2.
Physical properties of materials

Parameters	Molten steel	Oxygen	Water	Air
Density, ρ (kg/m^3)	7000	Ideal gas	1000	1.29
Viscosity, μ (Pa·s)	6.5×10^{-3}	1.19×10^{-5}	0.001	1.789×10^{-5}
Surface tension, σ (N/m)	1.6	-	0.071	-
Specific heat, C_P (J/kg·k)	670	919.31	4182	1006.43
Thermal conductivity, λ (W/m·k)	40	0.0246	0.6	0.0242
Temperature, T (K)	1873	300	300	300

2.5. Physical experiments and computational verification

Figure 2 shows the physical experimental model of a 260 Mg converter with a geometric similarity ratio of 1:7. the system included lifting platform, converter model, high-speed camera, air compressor, air tank, conductivity meter, computer, oxygen lance nozzle, etc. Oxygen and molten steel are simulated using compressed air and water, respectively.

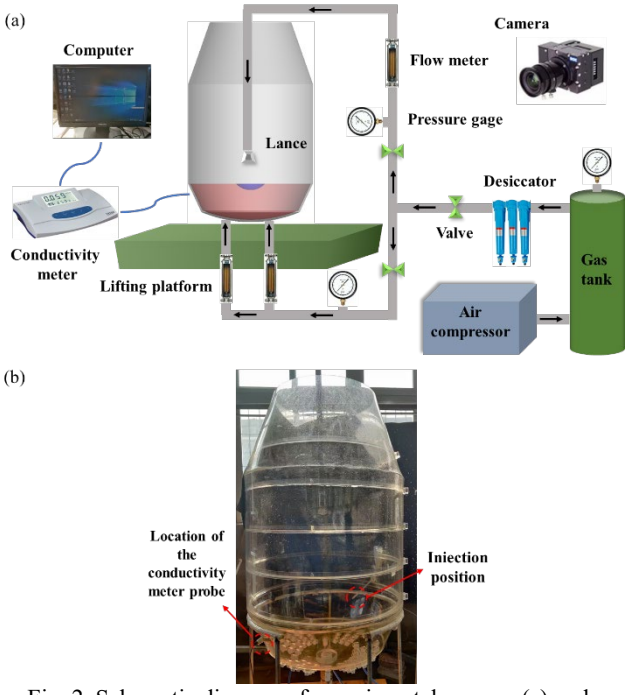

Fig. 2. Schematic diagram of experimental process (a) and converter model (b)

In the process of supersonic oxygen jet impacting the molten bath, the gravity of the molten steel and the inertial force of the gas have a decisive impact on the fluid flow in the model. In this study, the modified Froude number was used to calculate the experimental parameters [22]. The Froude number is modified as follows:

$$Fr' = \frac{\rho_g u_g^2}{gH\left(\rho_l - \rho_g\right)} \tag{9}$$

where u_g is the gas velocity at the nozzle outlet (m/s), ρ_g is the gas density at the nozzle outlet (kg/m^3), ρ_l is the liquid density (kg/m^3), g is gravitational acceleration (m/s^2), and H is the lance height (m). The model and prototype parameters were calculated based on the geometric and dynamic similarity, and the values of the parameters are listed in Table 1.

As shown in Figure 3, the shape of the cavity was captured by a high-speed camera and the size of the cavity was measured using Image J software. The maximum distance from the lowest point of the cavity to the liquid level of the molten bath was defined as the depth of the cavity, denoted by n_0. Due to the difficulty in measuring the impact area, the splashing diameter at the edge of the cavity is used as the cavity width, denoted by d_0. To minimize measurement errors, the average of five images was calculated under each operating condition as the final value. As shown in Figure 2, 200 mL saturated KCL solution was added to the converter after blowing for 30 s. A conductance probe was installed in the position, which is opposite to the direction of the additional position and on the side wall 200 mm away from the bottom of the converter. The conductance probe was used to monitor the conductivity of the liquid at 1 s intervals. After a period of time, the conductivity gradually stabilizes, and the time when the conductivity is within ±2.5% of the final value is defined as the mixing time. To reduce errors, the average of three measurements is taken as the final mixing time. Figure 4 compares the numerical simulated cavity depth with experimental cavity depth under different lance heights. H and d_e are respectively defined as oxygen lance height and outlet diameter of nozzle. H/d_e is a dimensionless quantity, which represents the distance between oxygen lance and molten bath. The maximum error is 5.5%, and the average error is 3.9%. Thus, the simulation and experimental results are in good agreement within the allowed errors.

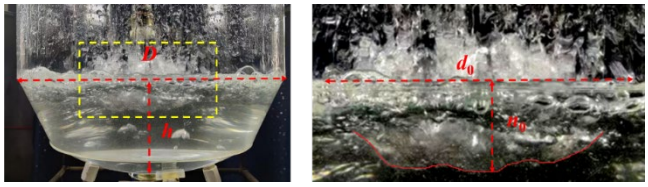

Fig. 3. Image processing to measure the cavity depth and width

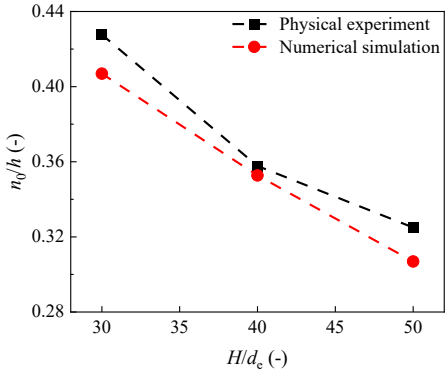

Fig. 4. Comparison of cavity depth between physical experiment and numerical simulation

3. Results and discussion

3.1. Physical experiment analysis

Cavity depth represents the impact strength of the jet, and also indirectly reflects the stirring ability of the jet on the molten bath. The contrast of cavity depth of the oxygen lance with various swirl angles at different flow rates and lance heights is shown in Figure 5. It can be seen that the cavity depth increases with the increase of flow rate or the decrease of lance height. This is because increasing the flow rate or decreasing the lance height both increase the jet velocity, thereby increasing the impact strength of the jet on the molten bath. When the lance height increases from 30 d_e to 50 d_e, the average depth of cavity decreases from 107.8 mm to 85.8 mm. In contrast, when the flow rate increases from 70 Nm^3/h to 90 Nm^3/h, the average depth of cavity increases from 101.4 mm to 114.3 mm. The results demonstrate that the effect of lance height on cavity depth is higher than that of flow rate. Therefore, it is necessary to adjust the lance height reasonably according to the smelting needs in the BOF (basic oxygen furnace) steelmaking. In

addition, it can be observed from Figure 5 that the cavity depth of swirl-type oxygen lance is lower than that of traditional oxygen lance, and it further decreases with the increase of swirl angle.

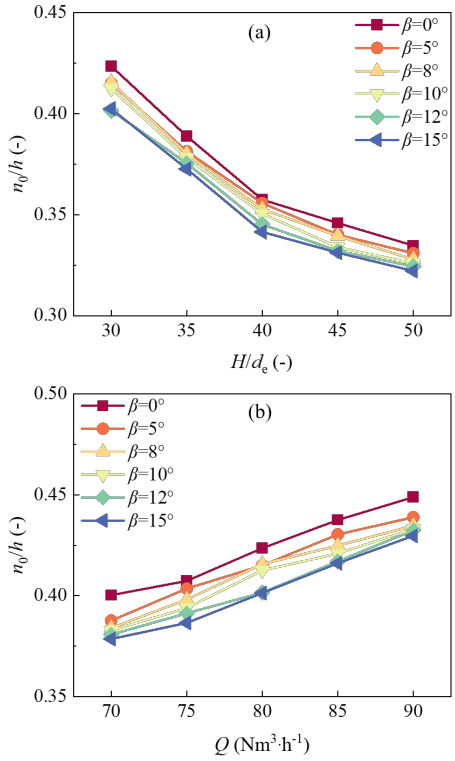

Fig. 5. The influence of swirling angle on cavity depth under different lance heights (a) and flow rates (b)

The contrast of cavity width of the oxygen lance with various swirl angles at different flow rates and lance heights is shown in Figure 6. It can be seen that the cavity width increases with the increase of flow rate and lance height. It indicates that increasing the lance height and flow rate can enhance the degree of contact between the jet and the molten bath surface, thereby enlarging the slag-steel reaction interface and increasing the metallurgical reaction rate. Besides, the cavity width increases with the increase of swirl angle. The result can be explained by the fact that the influence of jet coalescence is reduced due to swirl angle, resulting in the increase of the jet impact range.

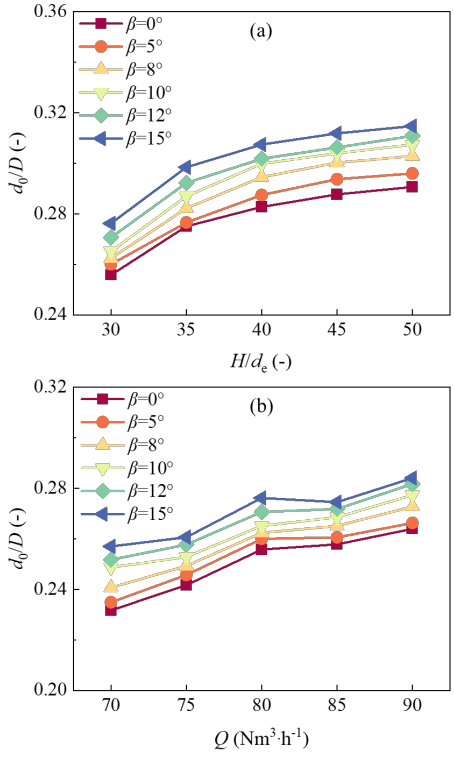

Fig. 6. The influence of swirling angle on cavity diameter under different lance heights (a) and flow rates (b)

The contrast of mixing time of the oxygen lance with various swirl angles at different flow rates and lance heights is shown in Figure 7. The results indicate that with the increase of flow rate and lance height, the mixing time first decreases and then increases, and the mixing time is lowest when H=40d_e or Q=80 Nm^3/h. The main reason is that when the lance height is lower or the flow rate is higher, the jet energy is mainly used to penetrate the molten bath and oscillate the liquid surface, causing that the edge of molten bath is not fully stirred. In contrast, the energy consumption of jet above the molten bath is too large to stir the molten bath when the lance height is higher or the flow rate is lower. In addition, it can be seen that the mixing time first decreases and then increases with the increase of swirl angle, and the mixing time is lowest at a swirl angle of 10 °. The reason is that the tangential momentum of swirl-type oxygen lance jet improves circumferential flow of molten steel and the mixing of molten bath. Nevertheless, excessive swirl angle accelerates the attenuation of jet velocity, which is adverse to the mixing of molten bath and increases the mixing time.

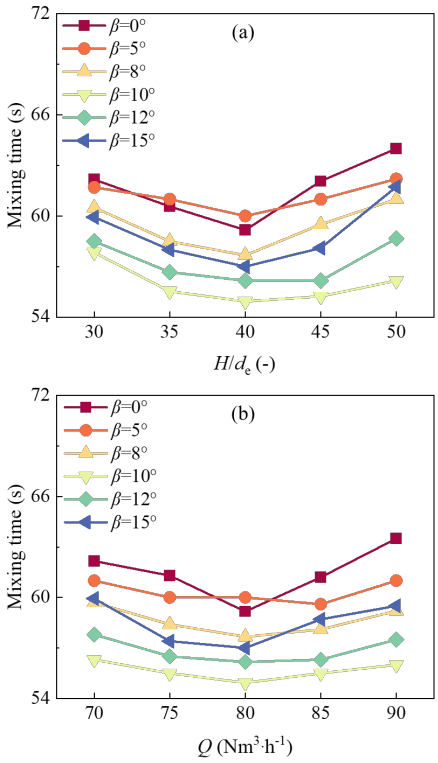

Fig. 7. The influence of swirling angle on cavity diameter under different lance heights (a) and flow rates (b)

3.2. Numerical simulation analysis

In the process of jets impact the molten bath, the violent energy exchange between jet and molten steel makes the molten bath flow. Figures 8 and 9 illustrate the velocity distribution of swirl angle of 0 °, 10 °, and 15 ° at different molten bath depths and radial distances under H=40d_e, respectively. The phenomena indicates that the increase of swirl angle increases the velocity at the upper of molten bath and equalizes the velocity at furnace wall. The results can be explained that swirl-type oxygen lance causes the increase of the impact width and the improvement of molten steel flow at the furnace wall. Furthermore, the stirring at the upper of molten bath is strengthened under the action of swirling jet.

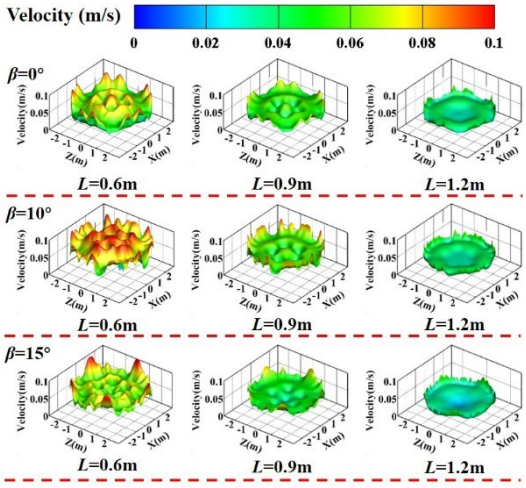

Fig. 8. Velocity distribution at different molten bath depths for swirl angle 0 °, 10 °, and 15 °

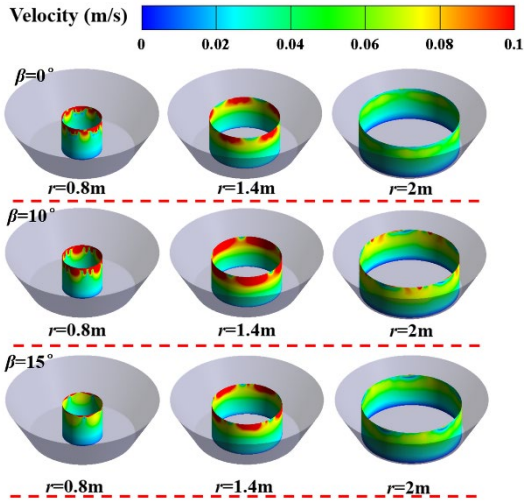

Fig. 9. Velocity distribution at different radial distances for swirl angle 0 °, 10 °, and 15 °

The corresponding area-averaged velocity on each section is quantified in Figure 10. These figures show that area-averaged velocity decreases with the increase of molten bath depth, but the area-averaged velocity at different radial distances first increases and then decreases with the increase of radial distance, reaching its maximum at r=1.4 m. These data indicate that the high-velocity zone is mainly distributed in the zone outside the center of molten bath. In addition, the area-average velocity of each section does not vary monotonously with the increase of swirl angle, but which achieve the maximum at the swirl angle of 10 °.

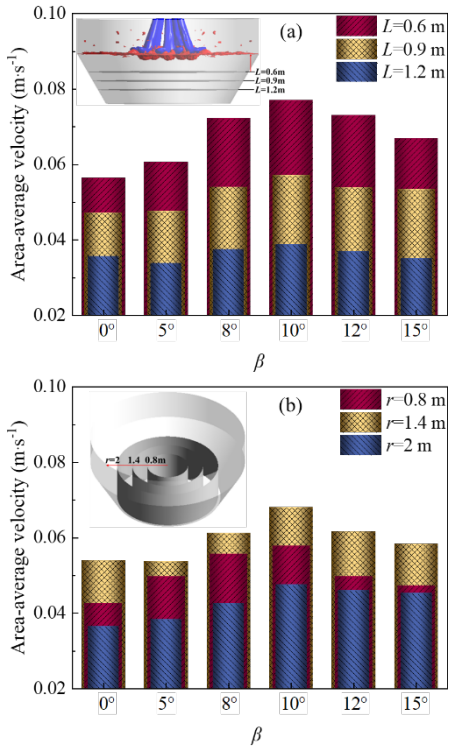

Fig. 10. Comparison of the area-average velocity on axial (a) and radial (b) section under different swirl angles

To further investigate the influence of swirl angle on the stirring effect of molten bath, the zone with a velocity of less than 0.03 m/s is defined as the dead zone, the zone with a velocity in the range of 0.03~0.1 m/s is defined as the weak flow zone, and the zone with a velocity higher than 0.1 m/s is defined as the active flow zone [23]. The distributions of velocity range of molten bath with various swirl angles under H=40d_e are shown in Figure 11. The red, blank, and blue zone of molten bath represent active flow zone, weak flow zone, and dead zone, respectively. It can be observed that compared to the traditional oxygen lance, the dead zone volume at the furnace wall of the swirl-type oxygen lance is significantly reduced. The phenomenon can be explained as follows, the increase of impact range of swirl-type oxygen lance makes molten steel more actively flow at the furnace wall, thereby reducing the dead zone volume.

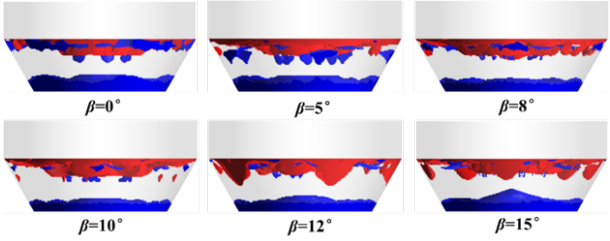

Fig. 11. Distribution of active flow zone, weak flow zone, and dead zone of molten bath under different swirl angles

Figure 12 shows that the volume of active flow zone first increases and then decreases with the increase of swirl angle, while the volume of dead zone is opposite to which. When the swirl angle is 10 °, the volume ratio of the active flow zone is the highest at 14.9%, and the volume ratio of the dead zone is the lowest at 11.8%. Compared with the traditional oxygen lance, the volumes of the active zone and the dead zone at swirl angle of 10 ° increased by 44.3% and decreased by 39.9% respectively. Furthermore, the volume-average velocity of molten steel first increases and then decreases. When the swirl angle is 10°, the maximum is 6.31×10^{-2} m/s. Overall, compared to the traditional oxygen lance, the stirring efficiency of the swirl-type oxygen lance jet on molten bath is improved by 5.5% to 16.8%.

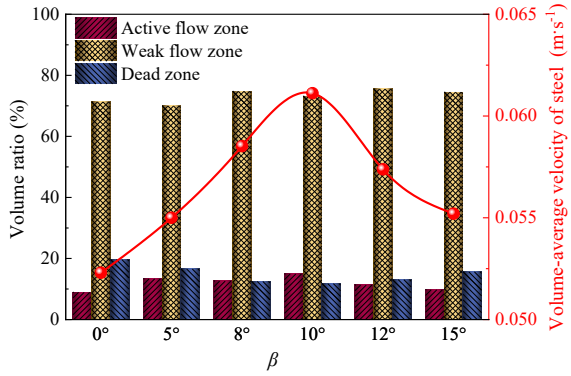

Fig. 12. Volume ratio of each zone and volume average velocity of steel of the molten bath for oxygen lance with different swirl angles

3.3. Industrial test

It has been found that the swirl-type oxygen lance can significantly improve the stirring effect of the molten bath by physical experiments and numerical simulations. To further verify the metallurgical effect of the swirl-type oxygen lance, industrial test was conducted on traditional oxygen lance (β=0 °) and swirl-type oxygen lance (β=10 °) on a 260 Mg converter. The dephosphorization rate, decarburization effect, and final slag composition of the molten steel were analyzed.

Figure 13 shows the dephosphorization rate and final carbon content of molten steel with different oxygen lances. As can be seen from Figure 13 (a), the dephosphorization rates of the traditional oxygen lance and the swirl-type oxygen lance are 78.9% and 81.2% respectively, with the latter increasing by 2.3% compared to the former. This is because the swirl-type oxygen lance increases the contact area between the jet and the slag, thereby effectively improving the slag-metal mixing, promoting the mass transfer of phosphorus elements at the slag-metal interface, and accelerating the dephosphorization reaction rate. Figure 13 (b) shows that the final carbon content of traditional oxygen lance and the swirl-type oxygen lance are 0.06% and 0.055% respectively. The main reason for this phenomenon is that the swirl jets enhance the flow of molten steel in the later stage of smelting, making the C-O reaction more vigorous.

Table 3 shows the final slag composition of different oxygen

lances. The results indicate that compared with traditional oxygen lance, the final slag phosphorus content of the swirl-type oxygen lance increases, the iron content of slag decreases by 0.11%. This means that the swirl-type oxygen lance reduces the consumption of converter metal materials and increases the metal yield.

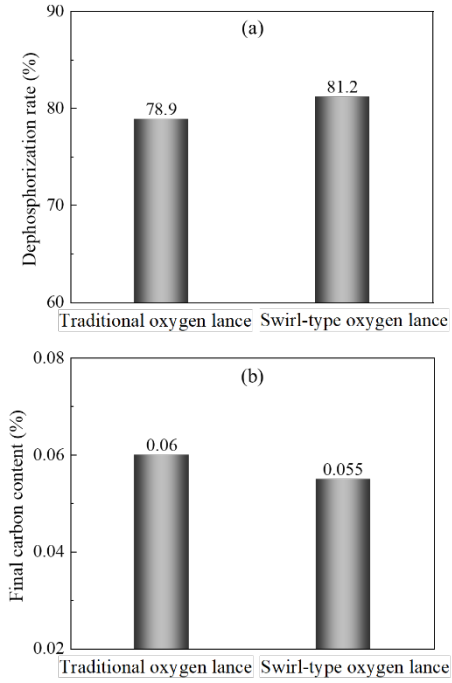

Fig. 13. Comparison of dephosphorization rate (a) and final carbon content (b) for different oxygen lances

Table 3.
Comparison of final slag composition of different oxygen lances

Parameters	Traditional oxygen lance	Swirl-type oxygen lance
CaO (%)	43.00	42.78
SiO_2 (%)	15.56	16.38
P_2O_5 (%)	1.79	2.09
Al_2O_3 (%)	6.26	6.49
MnO (%)	2.72	2.92
Fe (%)	13.12	13.01

4. Conclusions

1) Compared with traditional oxygen lance, the cavity depth, cavity width and mixing time of the swirl-type oxygen lance decrease, increase and decrease, respectively. The mixing efficiency of molten bath for swirl-type oxygen lance is improved by 5.5% to 16.8%.
2) The mixing time of the swirl-type oxygen lance decreases first and then increases with the increase of lance height and flow rate, and the mixing time is lowest when H=40d_e or Q=80 Nm^3/h.
3) When the swirl angle is 10 °, the shortest mixing time of the molten bath is 53.9 s; the maximum average velocity of the molten steel is 6.31×10^{-2} m/s, and the minimum dead zone volume ratio is 11.8%.
4) Compared with traditional oxygen lance, the swirl-type oxygen lance increased the dephosphorization rate by 2.3%, decreased the final carbon content by 0.005%, and decreased the iron content of final slag by 0.11%.

Acknowledgments.

The authors are grateful for the financial support by Innovation and Entrepreneurship Training Program for College Students and Project of Liaoning Provincial Department of Education (JYTMS20230932).

References

[1] Cai, X.Y., Duan, H.J., Ding, D.H., Xu, A.J. & Zhang, L.F. (2024). Water modeling on fluid flow and mixing phenomena in a BOF steelmaking converter. *Journal of Iron and Steel Research International*. 31(3), 595-607. DOI: 10.1007/s42243-023-01072-7.
[2] Burkert, J. & Schwarze, R. (2025). Analysis of surface behavior and cavity oscillations in a liquid metal model experiment of the basic oxygen furnace process. *Steel Research International*. 96(5), 2300184, 1-9. DOI: 10.1002/srin.202300184.
[3] Quiyoom, A., Ajmani, S.K. & Buwa, V.V. (2018). Optimization of bottom tuyere configuration for basic oxygen furnace steelmaking through experiments and CFD simulations. *Chemical Engineering Journal.* 346(1), 127-142. DOI: 10.1016/j.cej.2018.03.122
[4] Tago, Y. & Higuchi, Y. (2003). Fluid flow analysis of jets from nozzles in top blown process. *ISIJ international*. 43(2), 209-215. DOI: 10.2355/isijinternational.43.209.
[5] Alam, M., Naser, J. & Brooks, G. (2010). Computational fluid dynamics simulation of supersonic oxygen jet behavior at steelmaking temperature. *Metallurgical & Materials Transactions B*. 41(3), 636-645. DOI: 10.1007/s11663-010-9341-0.
[6] Sambasivam, R, Lenka, S.N., Durst, F., Bock, M., Chandra, S. & Ajmani, S.K. (2007) A new lance design for BOF steelmaking. *Metallurgical and Materials Transactions B*. 38(1), 45-53. DOI: 10.1007/s11663-006-9004-3.
[7] Lv, M., Zhu, R., Guo, Y.G. & Wang, Y.W. (2013). Simulation of flow fluid in the BOF steelmaking process. *Metallurgical & Materials Transactions B*. 44(6), 1560-1571. DOI: 10.1007/s11663-013-9935-4.
[8] Li, Q., Li, M. M., Kuang, S.B. & Zhu, R. (2014). Computational study on the behaviours of supersonic jets and their impingement onto molten liquid free surface in BOF steelmaking. *Canadian Metallurgical Quarterly*. 53(3), 340-351. DOI: 10.1179/1879139514y.0000000124.
[9] Ek, M. & Sichen, D. (2012). Study of penetration depth and droplet behavior in the case of a gas jet impinging on the surface of molten metal using liquid Ga – In – Sn. *Steel*

Research International. 83(7), 678-685. DOI: 10.1002/srin.201100336.

[10] Sabah, S. & Brooks, G. (2016). Energy balance around gas injection into oxygen steelmaking. *Metallurgical & Materials Transactions B*. 47(1), 458-466. DOI: 10.1007/s11663-015-0475-y.

[11] Li, M.M., Li, Q., Zou, Z.S. & An, X.Z. (2017). Computational investigation of swirling supersonic jets generated through a nozzle-twisted lance. *Metallurgical and Materials transactions B*. 48(1), 713-725. DOI: 10.1007/s11663-016-0851-2.

[12] Maia, B. T., Imagawa, R.K., Petrucelli, A.C. & Tavares, R.P. (2014). Effect of blow parameters in the jet penetration by physical model of BOF converter. *Journal of Materials research and Technology*. 3(3), 244-256. https://doi.org/10.1016/j.jmrt.2014.06.010.

[13] Yin, Z.C., LU, J.F., Li, Lin., Wang, T., Wang, R.H., Fan, X.H., Lin, H.K., Huang, Y.S. & Tan, D.P. (2020). Effect of blow parameters in the jet penetration by physical model of BOF converter. *Applied Sciences*. 10(15), 5101, 1-18. DOI: 10.3390/app10155101.

[14] Lv, M., Li, H., Lin, T.C., Xie, K. & Xue, K. (2021). Behavior of gas-slag-metal emulsion with nozzle-twisted lance in converter steelmaking process. *Steel research international*. 92(10), 2100103, 1-11. DOI: 10.1002/srin.202100103.

[15] Li, L., Li, M.M., Shao, L., Li, Q. & Zou, Z.S. (2020). Physical and mathematical modeling of swirling gas jets impinging onto a liquid bath using a novel nozzles-twisted lance. *Steel research international*. 91(7), 1900684, 1-7. DOI: 10.1002/srin.201900684.

[16] Liu, X., Xu, A.J., Yuan F. & Pang, C.B. (2023). Optimisation of the bottom blowing process for a 200t converter. *Ironmaking & Steelmaking*. 50(1), 1-12. DOI: 10.1080/03019233.2022.2078265.

[17] Munoz-esparza, D., Buchlin, J. M., Myrillas, K. & Berger, R. (2012). Numerical investigation of impinging gas jets onto deformable liquid layers. *Applied Mathematical Modelling*. 36(6), 2687-2700. DOI: 10.1016/j.apm.2011.09.052.

[18] Zhang, H., Yuan, Z.F., Mei, L., Peng, X., Liu, K. & Zhao, H.X. (2022). The behavior of CO_2 supersonic jets in the converter slag-splashing process. *Journal of Sustainable Metallurgy*. 8(4), 1803-1815. DOI: 10.1007/s40831-022-00607-8.

[19] Alam, M., Naser, J., Brooks, G. (2012) A computational fluid dynamics model of shrouded supersonic jet impingement on a water surface. *ISIJ international*. 52(6), 1026-1035. DOI: 10.2355/isijinternational.52.1026.

[20] Li, M.M., Li, L., Li, Q. & Zou, Z.S. (2018). Modeling of mixing behavior in a combined blowing steelmaking. *JOM: The Journal of the Minerals, Metals & Materials Society*. 70(10), 2051-2058. https://doi.org/10.1007/s11837-018-2889-x.

[21] Liu, Z., Cheng, S. & Peng, J. (2024). Simulation of fluid flow in the top–bottom combined blowing converter. *Metals*. 14(1), 56, 1-21. DOI: 10.3390/met14010056.

[22] Liu, G. Q., Liu, K. & Han, P. (2021). Splash sheet characteristics induced by the impingement of multiple jets in a steelmaking converter. *Ironmaking & Steelmaking*. 48(1), 25-32. DOI: 10.1080/03019233.2020.1720453.

[23] Sun, J.K., Zhang, J.S., Jiang, R., Feng, X.M. & Liu, Q. (2023). Effect of bottom tuyere arrangement based on impact cavity morphology on kinetic behavior of molten bath in converter. *Steel research international*. 94(1), 2200532, 1-14. DOI: 10.1002/srin.202200532.